Liquid Metal Shell as an Effective Iron Oxide Modifier for Redox-based Hydrogen Production at Intermediate-Temperatures

Iwei Wang[a,b], Yunfei Gao[a], Xijun Wang[a], Runxia Cai[a], Chingchang Chung[a], Sherafghan Iftikhar[a], Wei Wang[b,], Fanxing Li[a,*]*

[a] Department of Chemical and Biomolecular Engineering, North Carolina State University, 911 Partners Way, Raleigh, North Carolina 27695-7905, United States. * Email: fli5@ncsu.edu;

[b] School of Environment, Tsinghua University, Beijing, 100084, China. * Email: solid@tsinghua.edu.cn

KEYWORD. liquid metal, core-shell, chemical looping, hydrogen production, redox catalyst

ABSTRACT. This study reports molten metal (bismuth, indium, tin) as effective modifiers for iron-based redox catalysts in the context of chemical looping-based hydrogen production at intermediate-temperatures (450 °C-650 °C) from low calorific value waste gas (e.g. blast furnace gas). The effects of bismuth promoter on both surface and bulk properties of iron oxides were studied in detail. Transmission electron microscopy and energy dispersive spectroscopy (TEM-EDS), Low energy ion scattering (LEIS), Raman spectroscopy, and $^{18}O_2$ exchange experiment revealed that the bismuth modifier forms an overlayer covering the bulk iron (oxides), leading to better anti-coking properties compared to reference, $La_{0.8}Sr_{0.2}FeO_3$ and $Ce_{0.9}Gd_{0.1}O_2$ supported iron oxides. The Bi modified sample also exhibited improved anti-sintering properties and high redox activity, resulting in 4-fold increase in oxygen capacity compared to pristine Fe_2O_3 (28.9 wt.% vs. 6.4 wt.%) under cyclic redox reaction at 550 °C. Meanwhile, a small amount of bismuth is doped into the iron oxide structure to effectively enhance its redox properties by lowering the oxygen vacancy formation energy (from 3.1 eV to 2.1 eV) and the energy barrier for vacancy migration, as confirmed by experimental results and density functional theory (DFT) calculations. Reactive testing indicates that the Bi modified redox catalysts are highly active to convert low calorific value waste gases such as blast furnace gas. Our study also indicates that this strategy can be generalized to low-melting point metals such as Bi, In, and Sn for iron oxide modification in chemical looping processes.

1. INTRODUCTION

Iron and steel manufacturing is one of the most energy-intensive industrial subsectors, accounting for 7% of total direct global CO_2 emissions and around 5% global energy consumption.[1-2] An important approach to reduce the CO_2 emissions from the steel industry resides in efficient usage of its by-product gas such as blast furnace gas (BFG). BFG is composed of 0-28% CO, 1-5% H_2, 17-25% CO_2, and 50-55% N_2.[3] When burnt as fuel, BFG has a very low heating value (~ 0.9 kWh/Nm^3). This limits its

applicability for power generation. Therefore, BFG is often mixed with coke oven gas or flammable supports such as natural gas to sustain combustion.[4-5] This, however, further increases CO_2 emissions and the power generation efficiencies are limited. Carbon Capture and Storage (CCS) techniques can be used to reduce the CO_2 emissions from BFG combustion,[6-7] but state-of-the-art CCS technologies would add significant cost and energy penalties.[8-10] Therefore, efficient approaches to convert BFG or coke oven gas into clean energy carriers such as hydrogen is highly desirable.

Although hydrogen can be produced from BFG via water-gas-shift (WGS) reaction followed with gas separations, this conventional approach would be rather inefficient due to the presence of large amounts of N_2 and CO_2 in BFG. Chemical looping approaches, on the other hand, perform fuel conversion and water-splitting in separate steps, providing an inherently concentrated hydrogen product.[11-13] Originally proposed for CO_2 capture from fossil fuel combustion, the chemical looping gasification (CLG) or chemical looping water-splitting (CLWS) approaches have received increased attention.[14-16] Briefly, an oxide-based oxygen carrier is used to convert a fuel into hydrogen and/or heat via a cyclic redox process.[17-23]

Iron oxide is the most commonly investigated oxygen carrier for CLWS due to its high oxygen capacity and its suitable thermodynamic properties when compared to other first-row transition metal oxides.[24-27] Taking Fe_2O_3 as an example, Fe_2O_3 can be reduced by BFG to produce metallic Fe^0 in the reduction step. In the subsequent water-splitting step, the metallic Fe^0 can be re-oxidized with H_2O to produce Fe_3O_4 and H_2. Fe_3O_4 can be either directly used for the next redox cycle to react with BFG, or can be further re-oxidized with air in an additional re-oxidation step into Fe_2O_3. The theoretical oxygen capacity of Fe_2O_3 is 30 wt.% and its maximum usable capacity for H_2 production is 16.7 mol H_2/kg Fe_2O_3 per cycle, far exceeding any other oxygen carriers. However, while thermodynamically iron oxide is favored for the CLWS of BFG, iron-based oxygen carriers face a number of practical challenges such as sintering (mainly for the Fe^0 phase), coke deposition, and limited activity especially

at relatively low temperatures (<700 ºC).[24, 28-30] Deposition of iron oxide on an inert or mixed ionic-electronic conductive (MIEC) ceramic supports can enhance its redox activity and coke resistance.[31-37] However, this negatively impacts its oxygen carrying capacity.

Besides support materials, dopants of relatively small amount, i.e. <<10 wt.%, have also been used to increase Fe_2O_3's activity and stability. For example, Qin et al.[38-39] doped 1 wt.% of lanthanum oxide in Fe_2O_3 and found the reactivity and recyclability on CO combustion was improved without any significant change in the crystal phase and oxygen capacity after several redox cycles. The CO combustion reactivity increased by 233% and the air regeneration reactivity increased by 266% at 700 ºC on 1% La-doped oxygen carrier, since La dopants lower the barriers of the C-O bond activation. Chen et al.[40] investigated 1 at.% Ni and Cu doping effect in hematite and found that the dopants can significantly lower the energy barrier in both CH_4 and CO oxidation.

Despite of these promising findings, the coke formation and/or carburization on Fe^0 have received relatively little attention. This is an important issue in CLWS as any coke or carbide will be mostly converted to CO in the water splitting step. This not only affects the purity of H_2 product stream, but also adds limitations in applications such as proton exchange membrane (PEM) fuel cell as CO is a poison on the Pt catalyst. Moreover, further enhancement in the oxides' redox catalyst and coke resistance, especially at lower operating temperatures, are highly desirable.

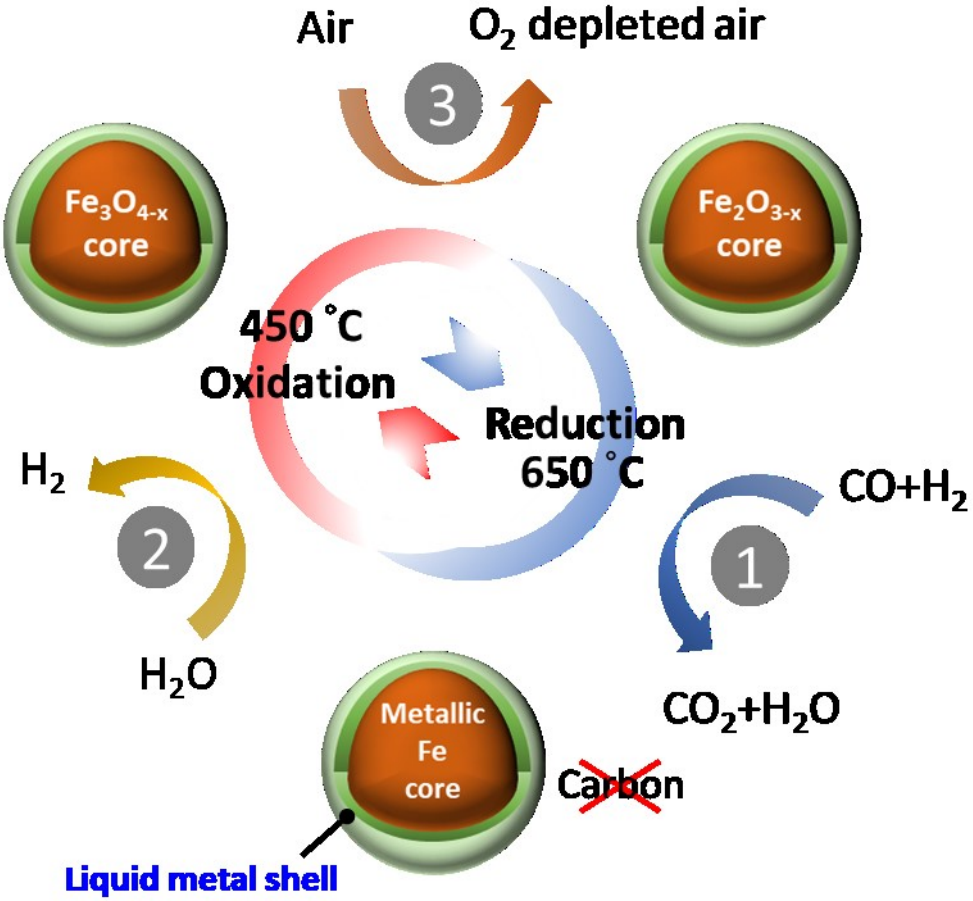

Figure 1. Simplified schematic of the chemical looping water-splitting process with liquid metal shells at intermediate-temperatures: (1) reduction with steel mill waste gas (CO + H_2), (2) steam oxidation for H_2 production, and (3) air oxidation to fully regenerate the iron oxide.

The present work reports low-melting point metals (LMPMs) modified iron oxide as effective redox catalysts for CLWS of low calorific waste gas (**Figure 1**). Different from the conventional, supported iron oxides, experimental tests, characterizations, and DFT calculations revealed that both surface and bulk of iron oxide are enhanced by merely 1 wt.% of LMPM promotion. Specifically, Bi enrichment on the oxide surface improved coke and sintering resistance whereas incorporation of a small amount of Bi (<<1 wt.%) in the bulk enhanced the reducibility of the oxide, as will be elaborated in a later section titled *effect of Bi-modification and redox reaction mechanism*. The influence of the

redox catalyst surface and bulk traits on the reactive performance displayed by bismuth-modified catalysts were thoroughly analyzed. The remarkable enhancements obtained by 1% Bi-Fe_2O_3 allows high oxygen capacity (~29 wt.%), excellent coke-resistance, and superior activity at intermediate-temperatures (450 °C-650 °C).

2. EXPERIMENTAL

Redox catalyst synthesis. All the redox catalysts were synthesized through a solid state reaction (SSR) method. The nominal compositions of these redox catalysts were summarized in **Table 1**. The SSR precursors include Fe_2O_3 (99.9%, Sigma-Aldrich), Bi_2O_3 (99.9%, Sigma-Aldrich), In_2O_3 (99.9%, Sigma-Aldrich), Sn_2O_3 (99.9%, Sigma-Aldrich), $La_{0.8}Sr_{0.2}FeO_3$ (LSF, Praxair Specialty Ceramics), and $Ce_{0.9}Gd_{0.1}O_2$ (GDC, Sigma-Aldrich). Stoichiometric amounts of LMPMs, MIEC ceramic supports or Fe_2O_3, and 20 to 30 Al_2O_3 grinding balls were added into a stainless steel jar. The jar was then sealed and ball-milled for one hour in a high-energy ball mill (JY7124-SWC). The material was finally collected and calcined in a tube furnace at 750 ºC for 8 h with airflow.

Table 1. Summary of the redox catalysts synthesized.

Sample no.	Composition (wt. %)
0.01% Bi-Fe_2O_3	0.01% Bi_2O_3, 99.99% Fe_2O_3
0.1% Bi-Fe_2O_3	0.1% Bi_2O_3, 99.9% Fe_2O_3
1% Bi-Fe_2O_3	1% Bi_2O_3, 99% Fe_2O_3
5% Bi-Fe_2O_3	5% Bi_2O_3, 95% Fe_2O_3
30% Bi-Fe_2O_3	30% Bi_2O_3, 70% Fe_2O_3
1% In-Fe_2O_3	1% In_2O_3, 99% Fe_2O_3
5% In-Fe_2O_3	5% In_2O_3, 95% Fe_2O_3
5% Sn-Fe_2O_3	5% Sn_2O_3, 95% Fe_2O_3

30% GDC- Fe_2O_3	30% $Ce_{0.9}Gd_{0.1}O_2$, 70% Fe_2O_3
30% LSF- Fe_2O_3	30% $La_{0.8}Sr_{0.2}FeO_3$, 70% Fe_2O_3
Fe_2O_3	100% Fe_2O_3

Redox catalyst characterizations. XRD data were obtained using a PANalytical Empyrean X-ray diffractometer with CuKα radiation (λ=1.5418 Å) in a 2 theta range of 15° to 80°. The step size and time per step used in these measurements are 0.013 degree and 298 sec/step, respectively. A Bragg-Brentano setup and a PIXcel1D detector were used during the data collection. A structural Rietveld refinement was performed to quantify the phase fractions, distributions and the lattice parameters in the samples using HighScore Plus software. The elemental compositions of the as-prepared redox catalysts were quantified by inductively coupled plasma optical emission spectrometry (ICP-OES, Agilent 720) and X -ray fluorescence (XRF) using an XRF-1800 Analyzer (Shimadzu Corp., Kyoto, Japan). High-resolution transmission electron microscope (TEM) images and energy dispersive spectroscopy (EDS) mappings were recorded on a STEM (FEI Talos F200) operated at 200 kV. Raman spectra were acquired on Horiba Jobin Yvon LabRam equipped with a CCD detector and a microscope with a 100 × objective lens. Low-energy ion scattering (LEIS) was conducted on 1% Bi-Fe_2O_3 and 1% Bi-Fe at the Surface Analysis Center at Lehigh University with an ION-TOF Qtac^{100} for surface compositional analysis and depth profiling. A 3 keV He^+ (1×10^{14} ions cm^{-2} cyc^{-1}, 1.5 × 1.5 mm raster) primary ion beam was used at 3000 eV pass energy, while a 0.5 keV sputtering source (1.0×10^{15} ions cm^{-2} cyc^{-1}, 2 × 2 mm raster) was used at 30° angle to the sample surface for depth profiling. During the spectra acquisition and sputtering, charge neutralization was invoked. $^{18}O_2$ isotope exchange experiments were conducted on 0.1% Bi-Fe_2O_3, Fe_2O_3 as described by our previous study. 50 mg of redox catalyst was loaded into a 1/4 in. O.D. x 1/8 in. I.D quartz U-tube reactor and was heated under a 5% $^{16}O_2$ flow balance Ar. Once reaching the temperature setpoint, 1 mL pulses of 5% $^{18}O_2$ was

injected into the reactor. A total of 2 pulses 2 min apart were injected. m/z = 34 and 36 were measured on a quadrapole mass spectrometer (QMS, MKS Cirrus II), to determine the amount of oxygen exchange in each pulse. Nitrogen (m/z = 28) was tracked in order to determine the integration limits for each pulse. A room-temperature pulse injection was used to determine a pulse where oxygen exchange did not occur. The initial tested was 450 °C, and the temperature was raised in 50 °C increments to 700 °C.

H_2-TPR, steam-TPO and isothermal reduction by syngas were conducted in a thermogravimetric analyzer (Q600 SDT, TA, USA) (TGA). Up to 20 mg powdery samples were loaded into the TGA. For H_2-TPR, hydrogen, a major component of syngas, was used for an initial evaluation. The sample was first heated from room temperature to 100 ºC at a ramping rate of 10 ºC min^{-1}, after which the temperature increased from 100 ºC to 650 ºC at a ramping rate of 5 ºC min^{-1} under a continuous flow of 10% H_2 (200 ml min^{-1}, balance Ar). For steam-TPO, the sample was first pre-treated at 550 ºC with H_2 for a full reduction and was then cooled back to 100 ºC under continuous flow of Ar. The chamber then increased from 100 ºC to 650 ºC at a ramping rate of 5 ºC min^{-1} under a continuous flow of 2 % steam generated from a water bubbler (200 ml min^{-1}, balance Ar). For the isothermal reduction experiment, the sample was first heated from room temperature to the desired reaction temperature at a ramping rate of 10 ºC min^{-1}. At the reaction temperature, the sample was reduced by flowing syngas (200 ml min^{-1}, balance Ar) continuously for 100 min. The heat conductivity signals were recorded with a thermal conductivity detector (TCD) in the TGA along with the mass change at the same time.

Redox experiments and phase segregation tests. Cyclic redox experiments were conducted using the TGA. On the H_2-O_2 cycle, the samples were first heated from room temperature to 550°C at a rate of 10 °C min^{-1}. Then, a continuous flow of 30% hydrogen (200 ml min^{-1}, balance Ar) was introduced into the chamber for 20 min as the reduction step. The chamber was then purged with Ar for 10 min. Then, a continuous flow of 10% O_2 (200 ml min^{-1}, balance Ar) was passed through the chamber for 20

min as the oxidation process and following another 10 mins N_2 purge prior to the initiation of another redox cycle. On the syngas-steam cycle using temperature swing, the samples were first heated from room temperature to 600°C at a rate of 10 °C min^{-1}. Then, a continuous flow of 25% syngas (200 ml min^{-1}, balance Ar) was introduced into the chamber for 20 min in the reduction step, and cooled back to 450 ºC under continuous flow of Ar. Then, a continuous flow of 2.34 % steam from bubbler (200 ml min^{-1}, balance Ar) was passed through the chamber for 150 min as the oxidation step. And the end the oxidation step, the chamber was heated up to 600°C to the initiation of another redox cycle. Phase segregation tests also carried out in a TGA. Iron-based redox catalyst was first heated from room temperature to 650 °C at a rate of 10 °C min^{-1}. Then, a continuous flow of 30% hydrogen (200 ml min^{-1}, balance Ar) was introduced into the chamber till the sample weight decreased to 89% of its original weight before reduction. Then, 200 mL min^{-1} of pure Ar was passed through the chamber and the chamber was cooled back to 500 ºC and was held at that temperature under Ar for 2 hours.

Computational details. First-principles simulations were performed at the DFT level implemented by the Vienna ab initio Simulation package (VASP)[41] with the frozen-core all-electron projector augmented wave (PAW) model[42] and Perdew-Burke-Ernzerhof (PBE) functions.[43] A kinetic energy cutoff of 450 eV was used for the plane-wave expansion of the electronic wave function, and the convergence criterions of force and energy were set as 0.01 eV Å−1 and 10^{-5} eV respectively. A Gaussian smearing of 0.1 eV was applied for optimizations. A k-point grid with a 4 × 4 × 2 Gamma-centered mesh for sampling the first Brillouin zone was chosen for Fe_2O_3 unit cell containing 30 atoms and a 7 × 7 × 7 Gamma-centered mesh was set for Bi unit cell containing 2 atoms. The strong on-site coulomb interaction on the d-orbital electrons on the Fe sites were treated with the GGA+U approach with U_{eff} = 4 eV.[44-45] The climbing image nudged elastic band (CI-NEB) method was applied for transition sate optimization.[46] The adsorption energies are computed with $E_{ads} = E_{sur} + E_{mol} -$

$E_{sur-mol}$, where E_{sur}, E_{mol}, $E_{sur-mol}$ represent the total energies of the pristine surface, the free-standing molecule, and the adsorbed configurations, respectively.

3. RESULTS AND DISCUSSION

Reactive performance of Bi modified iron oxides. To confirm the structural properties of the redox catalysts, XRD patterns of the as-prepared Bi-Fe redox catalysts were obtained (**Figure 2**). The characteristic peaks of the Fe_2O_3 phase were detected for the all the samples, and Bi_2O_3 phase was not observed. When Bi loading is above 5%, $Bi_2Fe_4O_9$ (Garnet phase) and $BiFeO_3$ (Perovskite phase) were formed. This is consistent with the Bi-Fe-O phase diagram.[47-48] With the exception of 30 wt.% Bi sample, the intensities of the Fe_2O_3 characteristic peaks remained nearly unchanged. A more detailed comparison of the peak positions indicates that the diffraction peaks in the Bi-modified redox catalysts systematically shifted towards slightly lower 2θ angles when compared to those of pure iron oxides. This indicates that a small fraction of bismuth cation can be doped into the iron oxide phase. Meanwhile, Rietveld refinements on the pure Fe_2O_3 and low Bi content redox catalysts (0.01%, 0.1%, 1%) indicate that the lattice parameter changes are very small but are systematically increased with increasing Bi content. For instance, the unit cell volume increased from 301.7 $Å^3$ (pure iron oxide) to 302.1 $Å^3$ (1% Bi-Fe_2O_3). Further details are summarized in **Table S1** and **Figure S1**. The low Bi content redox catalysts maintained a hexagonal close-packed structure of Fe_2O_3. Further information about the XRD spectra and Rietveld refinement results can be found in the supplementary file. The ICP and XRF results (**Table S2** and **S3**) confirm that the actual compositions of the samples are similar to their nominal values. Potential contamination from the ball milling process and the stainless-steel grinding jar is negligible. In order to determine if the bismuth modifier has an effect on the reactive performance, extensive reduction and oxidation experiments were performed on both pristine and Bi modified iron oxide redox catalysts.

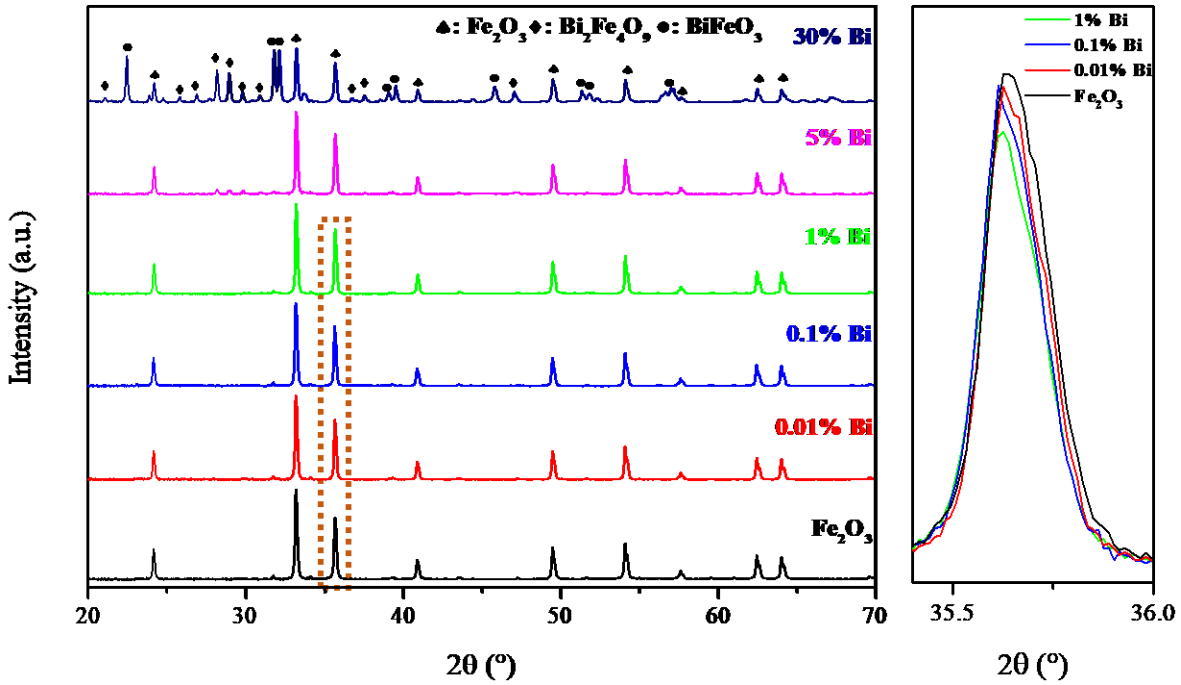

Figure 2. XRD patterns of the as-prepared Bi-Fe_2O_3 redox catalysts, and enlarged views of Fe_2O_3 peak shift of the (110) plane.

To determine their redox properties, H_2-TPR, steam-TPO, and isothermal reduction by syngas were performed on the redox catalysts. Reaction temperatures were limited to 650 °C given the focus was to enhance the redox activity at intermediate temperatures and to avoid volatilization of metallic bismuth for the high Bi loading sample. As shown in **Figure 3a**, all the as-prepared redox catalysts underwent a two-step reduction, which is indicative of $Fe_2O_{3(s)} \rightarrow Fe_3O_{4(s)} \rightarrow Fe^0_{(s)}$, and the weight loss curve was plotted in **Figure S2a**. Pristine Fe_2O_3 was reduced at 400 °C and 565 °C, respectively, and both peaks shifted to lower temperatures (~345 °C and ~530 °C) for the as-prepared Bi-Fe redox catalyst. Meanwhile, 1% Bi-Fe_2O_3 showed the lowest peak temperatures of 341 °C and 528 °C, respectively. This indicates that BiO_x effectively improves the oxygen ions migration from the bulk lattice to the surface. Notably, very low bismuth modified 0.01% and 0.1% Bi-Fe_2O_3 also exhibited enhanced reducibility. To verify the effect of Bi-doping and to rule out potential contaminants from

the ball milling process, a hand mixed 1% Bi-Fe_2O_3 redox catalyst was also prepared and evaluated with H_2-TPR (**Figure S2b and S2c)**. The hand mixed sample also showed demonstrably better performance than unmodified Fe_2O_3, confirming the effectiveness of the Bi modifier. Meanwhile, it is noted that the sample prepared with the high energy ball mill is slightly more active than hand mixed sample, this is likely to be due to better mixing of Bi and iron oxide. To determine the water-splitting properties of the redox catalysts, steam-TPO was conducted over pre-reduced 0.01%, 0.1%, 1%, 5% Bi-Fe redox catalysts and metallic iron (**Figure S2d**). As seen in **Figure 3b**, all redox catalysts underwent a one-step oxidation, which is indicative of $Fe^0_{(s)} \rightarrow Fe_3O_{4(s)}$, and the peak temperature for pure iron was 526 °C compared to 417 °C for 1% Bi-Fe. It is noted, however, that 5% Bi on Fe exhibited a higher peak temperature of 517 °C for water splitting, suggesting that higher bismuth loading hinders the activity.

Inhibition of coke formation by Boudouard reaction is another important challenge for efficient BFG or syngas conversion at intermediate temperatures. The reaction behaviors with 10% syngas (CO/H_2=1:2) are shown in **Figure 3c**. The redox catalysts showed a high reducibility and coke-resistance. Unlike Bi-Fe redox catalysts, pristine Fe_2O_3, GDC-Fe_2O_3, and LSF-Fe_2O_3 were not fully reduced by syngas due to thermal decomposition of CO which deposits carbon on the catalyst surface. This suggests that while MIEC modifier such as LSF and GDC could enhance reactivity significantly, both perovskite-type promoter and fluorite-type promoter could not suppress the severe coke formation at relatively low operating temperatures (550 °C) when compared to typical chemical looping reaction temperatures >800 °C. This is not surprising as Boudouard reaction is thermodynamically favored at lower temperatures. While iron oxides modified with ≥1wt.% Bi_2O_3 exhibit excellent coke resistance, coke formation was observed on 0.1% Bi-Fe_2O_3 after 10 min deep reduction, indicating that a minimum bismuth loading is required to effectively inhibit coking. Coke formation was further evaluated in a fixed-bed reactor at 550 °C (reduction in 25 vol % syngas balance Ar for 15 min, oxidation in 10 vol

% oxygen balance Ar for 15 min, shown in **Figure 3d**). Oxidation of pristine Fe_2O_3 reduced by syngas forms a large amount of CO and CO_2, indicating severe coking during the reduction in syngas. In contrast, coke formation on 1% Bi-Fe redox catalyst was not detectable. 1% Bi-Fe_2O_3 was further tested with a BFG simulant, with 25 vol % CO and H_2 at a 4:1 molar ratio balance Ar (**Figure S3)**. Excellent coke resistance was still observed. In summary, bismuth modifier shows outstanding performance on both surface and bulk of iron-based redox catalysts. The role of the bismuth modifier will be further discussed in the mechanistic section.

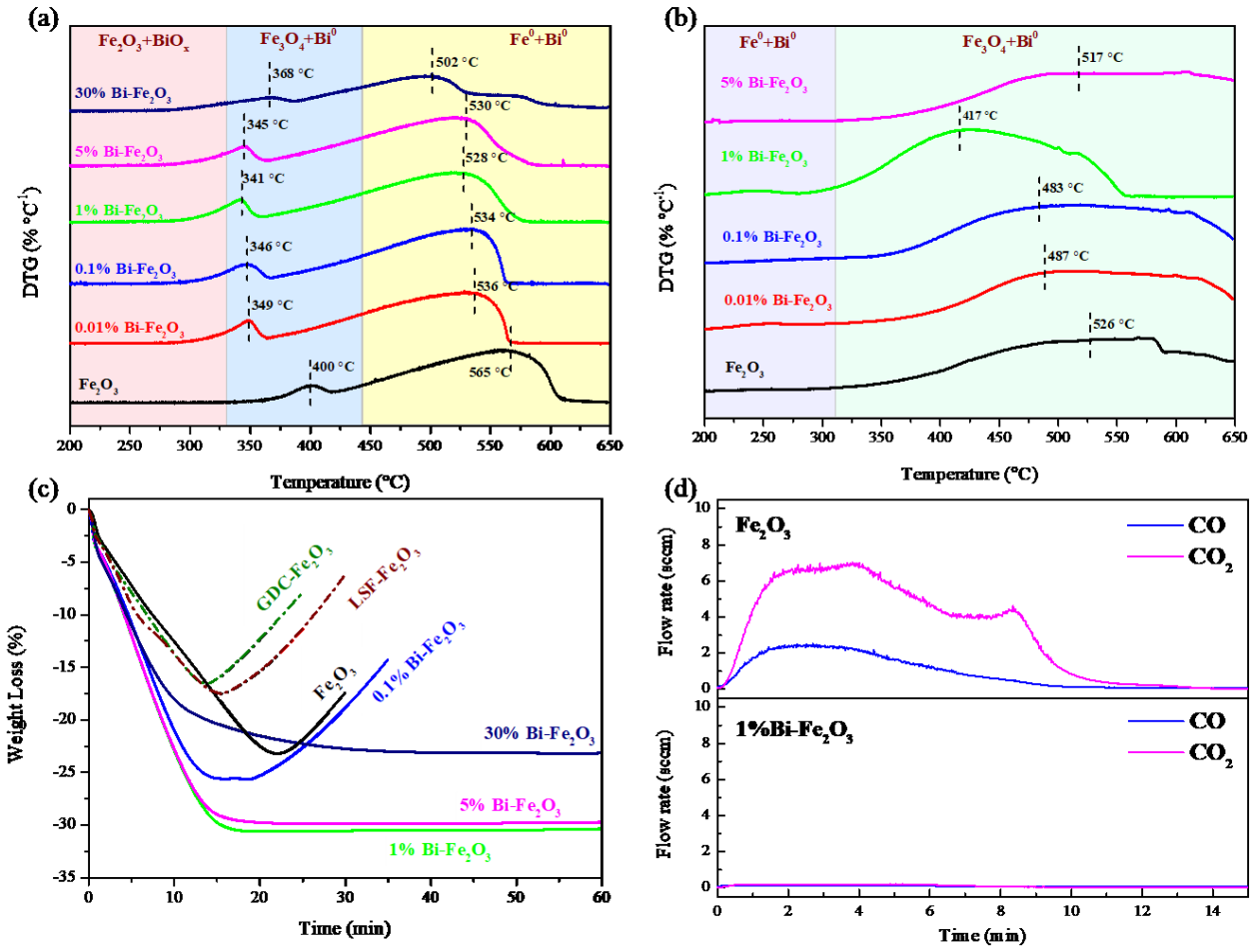

Figure 3. (a) DTG profile of H_2-TPR on as-prepared Bi-Fe_2O_3 redox catalysts; (b) DTG profile of steam-TPO on the Bi-Fe_2O_3 redox catalysts; (c) syngas reduction of as-prepared Bi-Fe_2O_3 redox

catalysts and reference catalysts at 550 °C; (d) CO_x evolution when oxidizing syngas reduced samples with O_2 in a packed bed reactor at 550 °C.

The cyclic redox performance of the redox catalysts was determined in TGA at 550 °C. **Figure 4a and 4b** plot the recorded changes in the sample mass during reduction (in H_2) and oxidation (in O_2) as a function of time. As can be seen, pure Fe_2O_3 exhibited notable deactivation over 10 cycles whereas 1% Bi-Fe_2O_3 redox catalyst remained active. This indicates that even at a relatively low redox reaction temperature, unmodified iron particles would still sinter, causing deactivation. This sintering induced deactivation was corroborated by XRD patterns as the re-oxidized iron oxide still exhibited obvious metallic iron peak (**Figure S4)**. In contrast, 1% Bi-Fe_2O_3 redox catalyst represents a 4-fold increase of oxygen capacity compared to unmodified Fe_2O_3 sample (28.9% vs. 6.4%) in 10^{th} H_2-O_2 redox cycle. This indicates that the presence of 1% Bi would be effective to greatly enhance the sintering resistance of iron oxide under redox conditions. Furthermore, the deactivated iron oxide, after reduction, has larger crystallite size (~37 nm) for Fe than freshly reduced iron oxide (~20 nm). This further indicates that re-oxidized iron oxide had severe sintering and the sintering was inhibited by the Bi layer on 1% Bi-Fe_2O_3. **Figure 4c and 4d** plot the changes in the sample mass during reduction (in BFG simulant) and oxidation (in steam) as a function of time. Both samples exhibited slight deactivation. This may have resulted from the inability of 2% steam, being a weak oxidant at low concentration, to fully re-oxidize the sample to Fe_3O_4 phase. This is consistent with the observation that a less than complete reduction in each step (80%, shown in **Figure 4d**), improved the redox stability of the sample. We also investigated H_2 stepwise and CO stepwise reduction for the 1% Bi-Fe_2O_3 sample in TGA (**Figure S5a**). The reduction rate of CO was fast than H_2, indicating that the Bi promoted redox catalyst can be quite effective for BFG conversion. Meanwhile, H_2/CO stepwise reduction and steam stepwise oxidation with *ex-situ* XRD confirm the presence of metallic Bi (**Figure S5b-c** and **Figure S6a-b**). This reveals that the Bi enriched on the surface would be liquid Bi metal under H_2/CO reduction and water re-

oxidation cycles, since the melting point of Bi is 271.4 °C. To verify the long-term performance, cyclic H_2-H_2O reactions were conducted over 60 cycles (**Figure S7**). Our instrumentation was limited to 2 vol.% steam injection and hence we adopted 50 shallow redox cycles followed 10 deep redox cycles to save time. While deactivation was observed initially, the redox activity was stabilized after 30 cycles and exhibited no obvious deactivation afterwards. Overall, satisfactory redox activity and oxygen storage capacity were maintained.

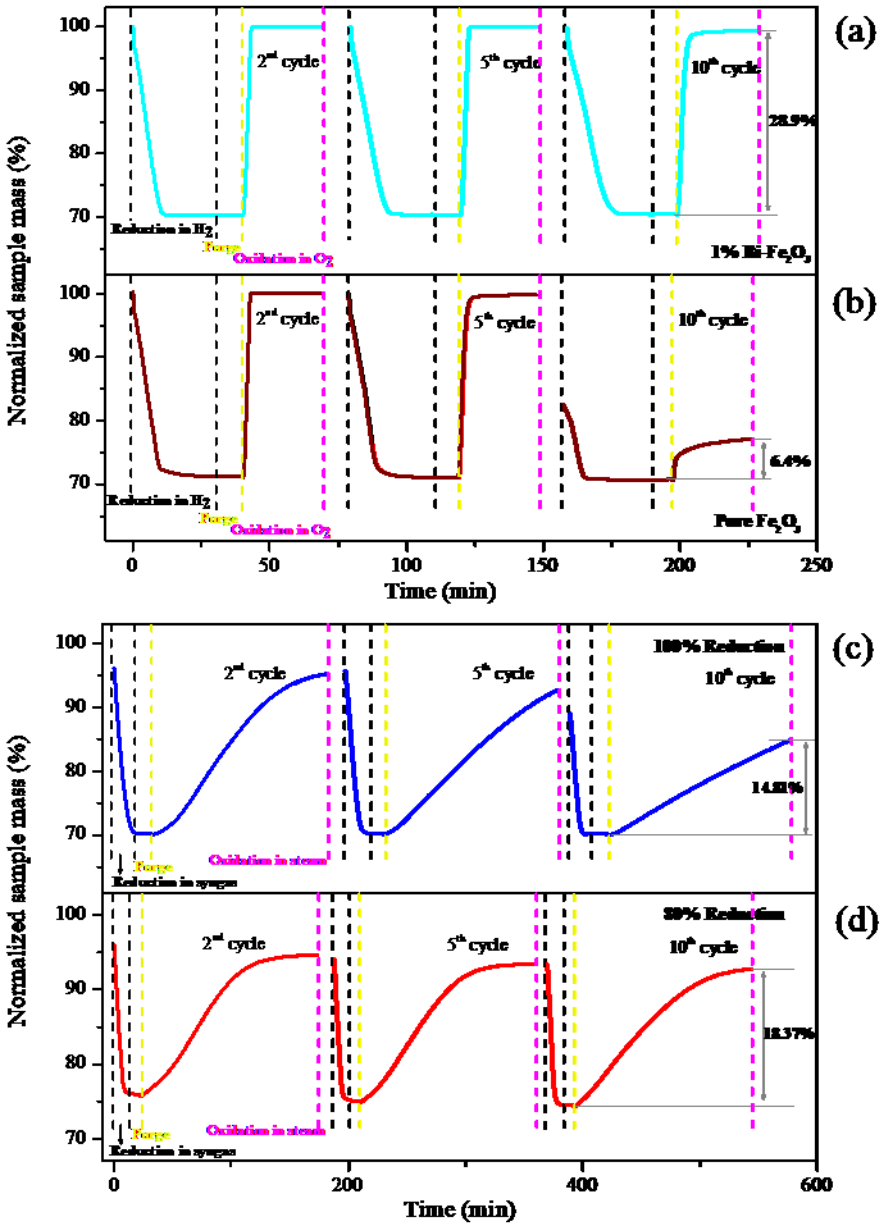

Figure 4. Sample mass as a function of time during H_2 reduction and oxygen oxidation in a TGA: (a) 1% Bi-Fe_2O_3 redox catalyst; (b) pure Fe_2O_3 sample. The experiments were performed at 550 °C using 30 % H_2 in Ar for reduction and at 550 °C using 10 % oxygen in Ar for oxidation. Sample mass as a function of time for 1% Bi-Fe_2O_3 redox catalyst during syngas reduction and steam oxidation in a TGA: (c) 100% reduction in syngas; (d) 80% reduction in syngas. The experiments were performed at 600 °C using BFG simulant, i.e. 25 % syngas (CO/H_2=4:1) in Ar, for reduction and at 450 °C using 2 % steam in Ar for oxidation.

Effect of Bi-modification and redox reaction mechanism. Given Bi's remarkable effectiveness to retard coke formation, sintering, and iron oxide deactivation, further characterizations were performed on Bi modified iron oxides. **Figure 5** shows a high-angle annular dark-field (HAADF) image and the corresponding EDS mappings of Fe and Bi of as-prepared 0.1%, 1%, 5% Bi-Fe_2O_3 and Fe, Bi, and C of 1% Bi-Fe reduced by syngas. The EDS mappings of as-prepared redox catalyst reveal a core-shell structure with bismuth enriching on the oxide surface. Similarly, the EDS mappings of 1% Bi-Fe reduced by syngas redox catalyst also present a core-shell structure. Both shell and core material showed insignificant carbon deposition. To further investigate the deposition of carbon on the reduced redox catalyst, Raman spectra was obtained on both 1% Bi-Fe and pure Fe_2O_3 reduced by syngas in **Figure S8**. Likewise, Raman spectra of 1% Bi-Fe reflected no carbon species on the material surface, which is consistent with the reactive performance and TEM results. In contrast, Raman spectra of pure Fe_2O_3 reflected carbon formation based on the D band and G band peaks at 1356 cm^{-1} and 1628 cm^{-1}, respectively.[49-50] To further verify the surface enrichment of Bi, LEIS was conducted to quantify the surface elemental composition and depth profiling of the redox catalysts. To identify the element distribution of each atomic layer of the redox catalysts, LEIS was conducted over as-prepared 1% Bi-Fe_2O_3 and 1% Bi-Fe reduced by H_2. In **Figure 6a**, on the as-prepared 1% Bi-Fe_2O_3 redox catalyst, LEIS spectra taken near the surface layer shows a large surface peak from Bi and sub-surface

background intensity from Fe, indicating Bi enrichment at the surface and a mixture of Bi and Fe in the bulk. For the further information on peak area and Bi/Fe ratio, **Figure S9a** shows high-concentration Bi throughout near-surface and Bi/Fe ratio decreases as a function of depth from 4.8 in the first layer to 1.6 in the 25th layer. On the 1% Bi-Fe reduced by H_2 redox catalyst in **Figure 6b**, Bi maintains a higher intensity, which is indicative of the surface enrichment, and Fe shows an increased intensity compared to as-prepared 1% Bi-Fe_2O_3. Additional sputtering shows increased amounts of Fe, yet Bi remained relatively the same; meanwhile, the peak area and Bi/Fe ratio remain a relatively stable curve (**Figure S9b**). Since the coking and sintering resistance are primary determined by the first few atomic layers, it has been shown that the bismuth layer on the surface benefits the redox performance.

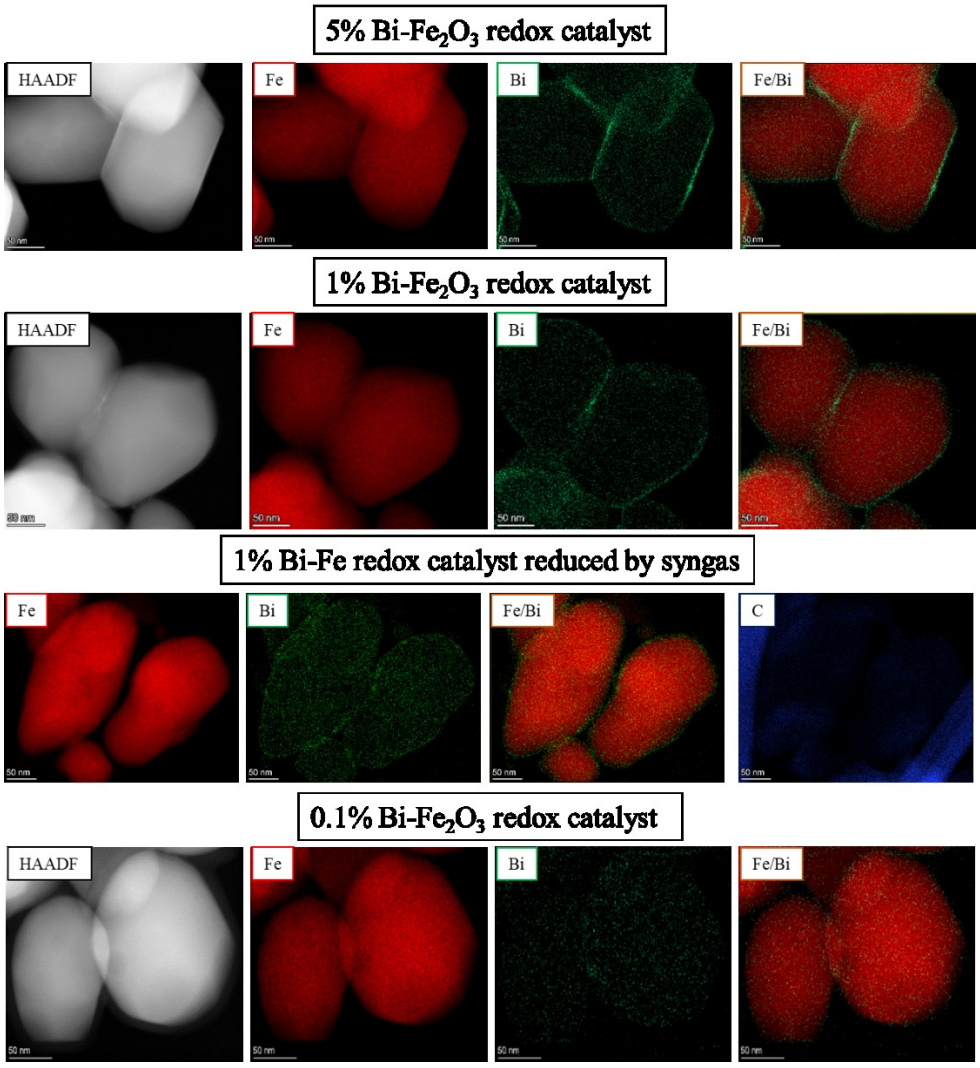

Figure 5. HAADF and elemental mapping of the as-prepared 0.1%, 1%, 5% Bi-Fe_2O_3 redox catalysts, the scale bar is 50 nm.

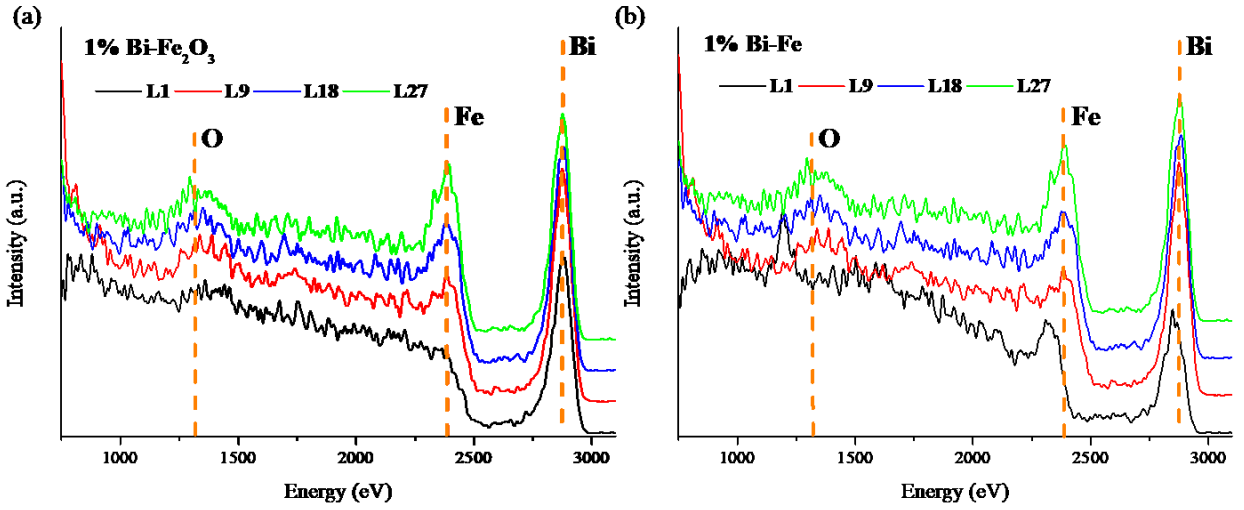

Figure 6. (a) LEIS spectra over sputter cycles on 1% Bi-Fe_2O_3; (b) LEIS spectra over sputter cycles on 1% Bi-Fe.

To further quantify the effect of surface Bi layer of the as-prepared Bi-Fe_2O_3 redox catalyst on oxygen exchange activity, $^{18}O_2$ pulsed isotopic exchange experiments based on the method reported by Bouwmeester et al.[51] were employed on as-prepared 0.1% Bi-Fe_2O_3 and pristine Fe_2O_3. Under an oxidizing environment, the surface would form a BiO_x layer. **Figure S10** shows the Arrhenius Plots of the overall surface oxygen exchange rate data. The activation energy for the overall rate of oxygen exchange was significantly higher on 0.1% Bi-Fe_2O_3 (101.3 kJ/mol) compared to pristine Fe_2O_3 (64.4 kJ/mol). This may contribute to slower rate of heat release from the oxidation reaction and hence decreased sintering. We note that the O_2 isotope exchange experiment can only be performed on fully oxidized sample since reduced sample will take up the oxygen isotope. Therefore, the results cannot provide information with respect to the effect of liquid Bi, which would present on the surface after the reduction and H_2O re-oxidation. The bismuth layer inhibits the overall exchange activity on the catalyst surface by limiting the dissociative adsorption of O_2. This further confirm the effect of Bi_2O_3

as a surface modifier of the iron oxide, which can retard sintering. Meanwhile, DFT calculations were performed to investigate the effect of the Bi overlayer. Adsorption of CO and H_2O molecules on the close-packed surfaces of Fe (110) and Bi(111) was considered, as shown in **Figure S11a** and **S11b**, respectively. The results indicate stronger adsorption energy for H_2O on the Fe(110) surface (E_{ads} = 0.33 eV) when compared to that on the Bi(111) surface (E_{ads} = 0.11 eV). Similarly, CO adsorption on Fe(110) (1.94 eV) is much stronger than that on Bi(111) (0.04 eV). From the reaction standpoint, the weakened CO adsorption on the Bi surface inhibits the contact between reducing gas (CO) and Fe, surpassing the Boudouard reaction and hence inhibiting coke formation as demonstrated experimentally. Meanwhile, surface enrichment of Bi in both reduced and oxidized forms of the redox catalysts indicates that the redox reactions are likely to proceed via lattice oxygen migration through the bismuth layer, as opposed to the migration of iron atom or cations. This is consistent with DFT calculations, which indicate significant energy barrier uphill (3.20 eV) for iron migration from Fe surface to the inner layer of Bi. (**Figure 7a**). The energy barrier, which is already prohibitively high at 0 K, can be even larger under experimental conditions due to two reasons: (1) the interatomic distance of molten Bi is closer than that of crystalline Bi,[52] making Fe harder to migration through the Bi layer; (2) the movement of the Bi atoms in molten Bi is likely to further retard iron migration through Bi. Therefore, the surface enriched Bi can serve as a protective layer to retard sintering resulted from Fe migration, as confirmed by cyclic redox experiments **(Figure 4)** and X-ray diffraction results **(Figure S4)**. In terms of water-splitting, due to the stronger interactions with H_2O molecule, Fe(110) can more effectively catalyze the H_2O splitting, with a low energy barrier of 0.77 eV, which is much lower than that catalyzed by Bi(111) (1.75 eV) (**Figure 7b**). This explains the lower steam-TPO activity for 5% Bi-Fe_2O_3 than that for 1% Bi-Fe_2O_3. Overall, 1% Bi-Fe_2O_3 provides a balance among (a) sintering resistance; (b) coke resistance; (c) and water-splitting activity. We note that the current DFT calculations on the Bi layer, which aim to explore the ease of Fe migration through the Bi layer and the preference of water splitting, used crystalline Bi as opposed to liquid Bi as the basis. Nevertheless,

these results can provide useful information with respect to the relative energy trends considering that the enthalpy change of molten Bi to crystalline Bi is merely 0.12 eV.

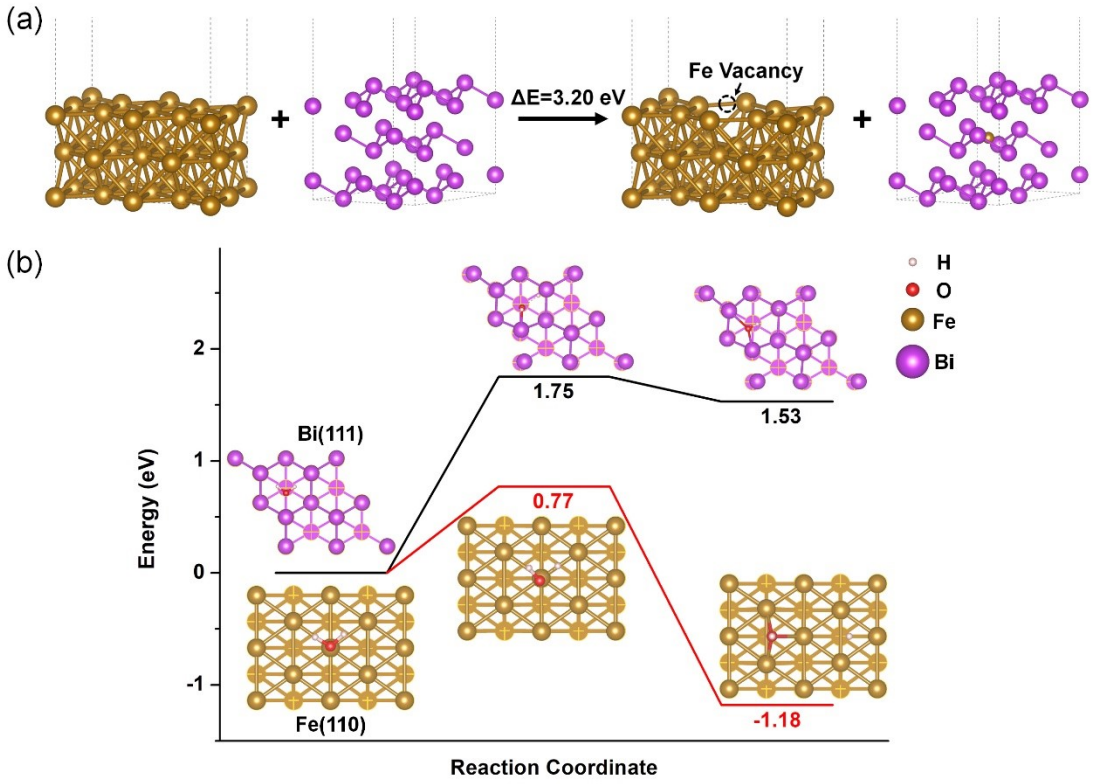

Figure 7. (a) Computed reaction energy of Fe atom migration from Fe surface to the inner layer of Bi. (b) Computed energy profiles of H_2O splitting on Fe(110) and Bi(111).

While Bi is enriched on the surface, XRD and depth profiling via LEIS also indicate that a small amount of Bi was doped into the iron oxide structure. To gain additional fundamental insights on the dopant effect of Bi, DFT calculations were performed to explore the impact of Bi dopants on the formation and diffusion of oxygen vacancy in bulk Fe_2O_3. The computed lattice constants of Fe_2O_3 bulk (a = 5.114 Å, b = 5.114 Å, c = 13.837 Å) agreed well with the experimental values (a = 5.038 Å, b = 5.038 Å, c = 13.772 Å). The model of Bi-doped Fe_2O_3 was constructed by replacing one Fe cation in pristine Fe_2O_3 with a Bi cation (**Figure S12**). The computed vacancy formation energy for the Bi-doped Fe_2O_3 is 2.11 eV, which is notably lower than that for pristine Fe_2O_3 (3.11 eV), shows that Bi

dopant facilitates iron oxide reduction. After Bi-doping, the migration of the lattice oxygen adjacent to the Bi cation is sterically hindered, as evidenced by the high energy barrier of 2.86 eV (**Figure 8**). However, for most oxygen sites away from Bi, the barrier for oxygen vacancy migration is enhanced with a slightly lower barrier of 1.13 eV compared with that in pristine Fe_2O_3 (1.22 eV). In summary, the presence of Bi dopant facilitates the reduction of iron oxide.

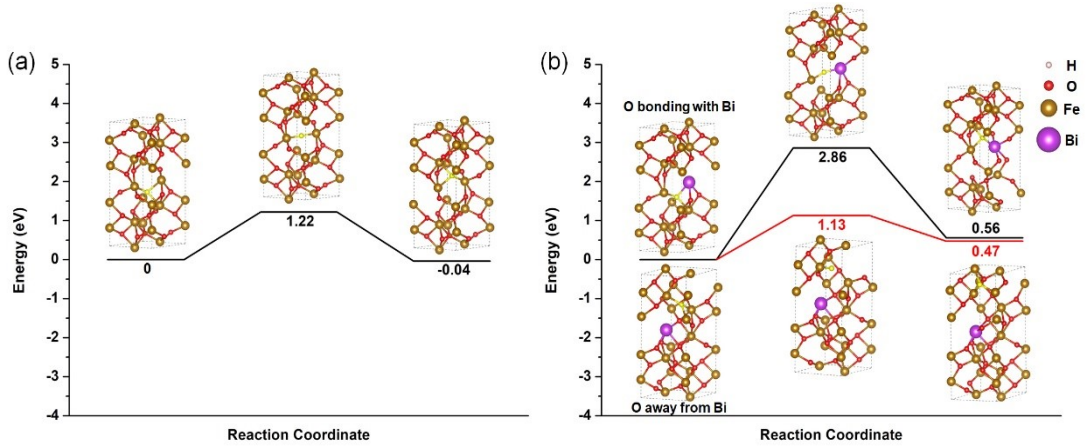

Figure 8. Computed energy profiles of oxygen migration in (a) pristine Fe_2O_3 and (b) Bi-doped Fe_2O_3.

Generality of the surface modification strategy. We found that the general concept of using a molten metal to enhance the redox properties of iron oxides can be extended to other systems. In-Fe_2O_3 and Sn-Fe_2O_3 redox catalysts were prepared and tested. For the LMPMs, the melting points of bismuth, indium and tin are 271.41 °C, 156.60 °C and 231.93 °C, respectively. Firstly, H_2-TPR was performed to characterize the reducibility of redox catalysts. As shown in **Figure 9a and S13a**, the H_2-TPR profiles of pure Fe_2O_3 exhibit extended reduction peaks and higher peak temperatures when compared to Bi, In, Sn-Fe_2O_3 redox catalysts. This indicates that small amounts of In and Sn also enhance the reducibility of iron oxide. These redox catalysts also showed a high reducibility and coke-resistance when reacting with BFG simulant (**Figure S13b)**. A likely explanation for the improved coke-resistance would be the liquid metal enrichment layer formed a coke-resistant layer, similar to Bi. To further evaluate the performance in water-splitting, **Figure 9b and S13c** compare the steam-TPO

performance on 1%, 5% Bi-Fe and In-Fe redox catalysts. On the steam-TPO curve, there was only one peak between 100 °C and 650 °C, indicating one oxidation step, $Fe^0_{(s)} \rightarrow Fe_3O_{4(s)}$. Notably, only 1% Bi-Fe had an obvious peak shift on steam oxidation, and according to the reaction curve, 5% In-Fe performed better than 1% In-Fe. **Figure S13d-f** plot the H_2-O_2 cycle on Indium modified redox catalysts. Unlike Bi-promoted sample, both In and Sn promoted Fe_2O_3 exhibited deactivation after oxygen regeneration. XRD indicates that sintering of Fe took place in both samples (**Figure S13f**) but the extents of sintering are less severe compared to unmodified iron oxide (**Figure S4**). This indicates that bismuth was the most effective promoter among the molten metals investigated.

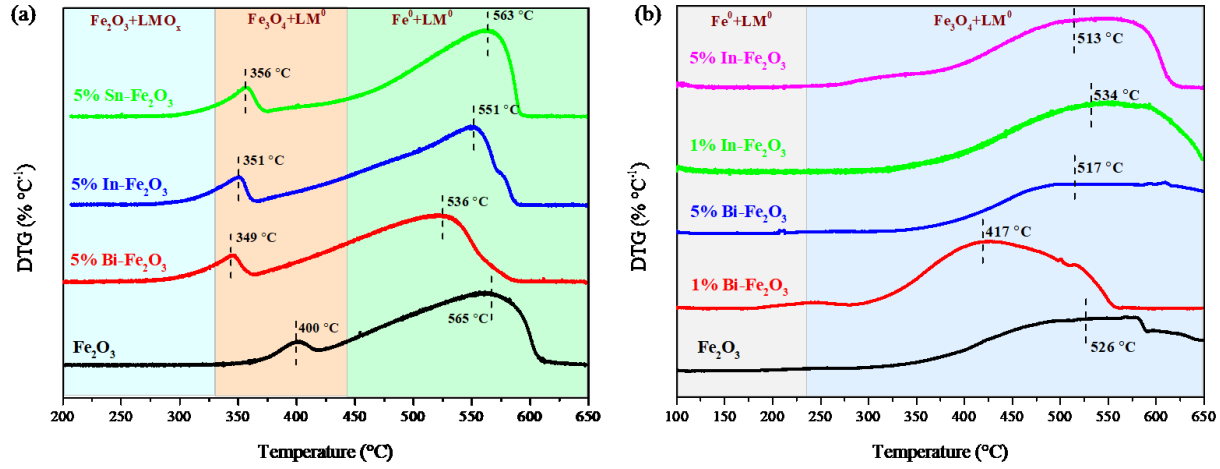

Figure 9. (a) DTG profile of H_2-TPR on as-prepared Bi, In, Sn-Fe_2O_3 redox catalysts; (b) DTG profile of steam-TPO on Bi, In-Fe redox catalysts.

Process implications. The higher activity for 1%Bi-Fe_2O_3 syngas conversion and particularly for water-splitting at relatively low temperatures offers interesting opportunities for effective BFG to hydrogen conversion. Among iron (oxides), metallic iron is the most effective phase for water-splitting whereas Fe_3O_4 and Fe_2O_3 are required for effective syngas conversion.[14] However, reduction of iron oxides often leads to FeO, as opposed to Fe, resulting from the difficulty to achieve both the highest oxidization states (Fe_3O_4/Fe_2O_3) and the lowest oxidation state (Fe) in a simple redox loop. Meanwhile, the lack of Fe would severely limit the steam to hydrogen conversion and hence the process efficiency.

By lowering the temperature of a partially reduced 1% Bi-Fe_2O_3 redox catalyst from 650℃ to 500℃, the wustite ($Fe_{1-x}O$) phase spontaneously transforms to metallic iron and magnetite (Fe_3O_4) phases (**Figure S14a-c**). While this is consistent with the phase diagram of iron oxides, such transition tends to be extremely slow in the absence of Bi dopant. Converting FeO to Fe phase at lower operating temperatures would greatly increase the steam to hydrogen conversion (K = 6.2 at 437℃, i.e. the steam TPO peak temperature for 1% Bi-Fe_2O_3). The water-splitting step would also fully re-oxidize Fe to Fe_3O_4 (**Figure 3b**). The resulting Fe_3O_4 can be quite effective for BFG conversion at higher operating temperatures ($\Delta G < 0$ at $T \geq 700$ C). Introduction of a small amount of air prior to the BFG conversion step can further facilitate full combustion of the BFG. The unique operational options offered by Bi modified iron oxide thus create interesting opportunities for efficiency enhancement for BFG conversion.

4. CONCLUSIONS

The present study investigates the effect of liquid metal (Bi, In, Sn) modifiers on iron oxide-based redox catalysts for blast furnace gas (BFG) conversion via a chemical looping approach. Specifically, 1 w.t.% Bi modified Fe_2O_3 led to a 4-fold increase in oxygen capacity compared to unmodified Fe_2O_3. The 1 w.t.% Bi Fe_2O_3 exhibited excellent performance for BFG (CO/H_2=4:1) conversion, water-splitting, and air reoxidation during the cyclic redox reactions. Detailed characterization revealed that a Bi overlayer covers the iron (oxide) substrate, which effectively retards the Boudouard reaction during the BFG conversion step and inhibits the sintering of the iron oxide particles. Besides surface enrichment, a small number of Bi cations are substituted into the bulk structure of the iron oxides, enhancing their redox activity. DFT calculations corroborated with the experimental findings and characterizations. First, CO adsorption on the Bi overlayer is significantly less favorable energetically, thereby inhibiting the Boudouard reaction. Moreover, Fe migration into the Bi surface layer is a highly endothermic process (3.2 eV). This retards the sintering of the iron oxide particles during the cyclic

redox reactions, especially for the highly exothermic iron oxidation step. Moreover, Bi doping in Fe_2O_3 not only lowers the oxygen vacancy formation energy by 1 eV but also slightly lowers the energy barrier for oxygen vacancy migration, leading to superior redox activity. Besides the Bi based modifier, we also demonstrated that similar effects can be extended to other liquid metals such as In and Sn, making it a generalized strategy to enhance iron oxides' redox performance in the context of water splitting and chemical looping reactions.

ASSOCIATED CONTENT

Supporting Information.

Supporting Information is available free of charge on the ACS Publications website. The supporting information includes Rietveld Refinement, ICP and XRF results of as-prepared redox catalysts, H_2-TPR, steam-TPO, isothermal reduction, H_2/CO stepwise reduction, steam stepwise oxidation, H_2-H_2O cyclic redox reaction, Raman spectra, LEIS spectra, $^{18}O_2$ pulsed isotopic exchange experiment, DFT calculations, XRD pattern of H_2-O_2 cycle and phase segregation.

AUTHOR INFORMATION

Corresponding Authors

Fanxing Li – Department of Chemical and Biomolecular Engineering, North Carolina State University, Raleigh, North Carolina 27695-7905, United States;

* Email: fli5@ncsu.edu

Wei Wang – School of Environment, Tsinghua University, Beijing, 100084, China;

* Email: solid@tsinghua.edu.cn

Authors

Iwei Wang– School of Environment, Tsinghua University, Beijing, China

Yunfei Gao – Department of Chemical and Biomolecular Engineering, North Carolina State University, Raleigh, North Carolina 27695-7905, United States

Xijun Wang – Department of Chemical and Biomolecular Engineering, North Carolina State University, Raleigh, North Carolina 27695-7905, United States

Runxia Cai – Department of Chemical and Biomolecular Engineering, North Carolina State University, Raleigh, North Carolina 27695-7905, United States

Chingchang Chung – Department of Chemical and Biomolecular Engineering, North Carolina State University, Raleigh, North Carolina 27695-7905, United States

Sherafghan Iftikhar – Department of Chemical and Biomolecular Engineering, North Carolina State University, Raleigh, North Carolina 27695-7905, United States

Notes

The authors declare no competing financial interest.

ACKNOWLEDGMENT

This work was supported by the U.S. National Science Foundation (Award No. CBET-1923468), and the Kenan Institute for Engineering, Technology and Science at NC State University. The authors acknowledge the use of the Analytical Instrumentation Facility (AIF) at North Carolina State University. The support provided to Iwei Wang by the Tsinghua Scholarship for Overseas Graduate Studies is also acknowledged.

REFERENCES

(1) Liu, X.; Chen, L.; Qin, X.; Sun, F. Exergy Loss Minimization for a Blast Furnace with Comparative Analyses for Energy Flows and Exergy Flows. *Energy*. **2015,** 93, 10-19.
(2) IEA. Global Energy & CO_2 Status Report 2019. *IEA*. Paris. **2019**.

(3) Carpenter, A. CO_2 Abatement in the Iron and Steel Industry. *IEA Clean Coal Centre*. **2012**, 67-70.
(4) Bojic, M.; Mourdoukoutas, P. Energy Saving Does Not Yield CO_2 Emissions Reductions: the Case of Waste Fuel Use in a Steel Mill. *Applied thermal engineering*. **2000,** 20, 963-975.
(5) Hou, S.; Chen, C.; Chang, C.; Wu, C.; Ou, J.; Lin, T. Firing Blast Furnace Gas without Support Fuel in Steel Mill Boilers. *Energy Conversion Management*. **2011,** 52, 2758-2767.
(6) Mousa, E.; Lundgren, M.; Ökvist, L. S.; From, L.-E.; Robles, A.; Hällsten, S.; Sundelin, B.; Friberg, H.; El-Tawil, A. Reduced Carbon Consumption and CO_2 Emission at the Blast Furnace by Use of Briquettes Containing Torrefied Sawdust. *Journal of Sustainable Metallurgy*. **2019,** 5, 391-401.
(7) Orre, J.; Ökvist, L. S.; Bodén, A.; Björkman, B. Understanding of Blast Furnace Performance with Biomass Introduction. *Minerals*. **2021,** 11, 157.
(8) Lockwood, T. A Compararitive Review of Next-Generation Carbon Capture Technologies for Coal-Fired Power Plant. *Energy procedia*. **2017,** 114, 2658-2670.
(9) Görke, R.; Hu, W.; Dunstan, M.; Dennis, J.; Scott, S. Exploration of the Material Property Space for Chemical Looping Air Separation Applied to Carbon Capture and Storage. *Applied energy*. **2018,** 212, 478-488.
(10) Yan, Y.; Wang, K.; Clough, P. T.; Anthony, E. Developments in Calcium/Chemical Looping and Metal Oxide Redox Cycles for High-Temperature Thermochemical Energy Storage: A Review. *Fuel Processing Technology*. **2020,** 199, 106280.
(11) He, F.; Li, F. Perovskite Promoted Iron Oxide for Hybrid Water-Splitting and Syngas Generation with Exceptional Conversion. *Energy & Environmental Science*. **2015,** 8, 535-539.
(12) Hosseini, D.; Donat, F.; Kim, S. M.; Bernard, L.; Kierzkowska, A. M.; Müller, C. R. Redox-Driven Restructuring of FeMnZr-Oxygen Carriers Enhances the Purity and Yield of H_2 in a Chemical Looping Process. *ACS Applied Energy Materials*. **2018,** 1, 1294-1303.
(13) Voitic, G.; Hacker, V. Recent Advancements in Chemical Looping Water Splitting for the Production of Hydrogen. *Rsc Advances*. **2016,** 6, 98267-98296.
(14) Fan, L.-S.; Li, F. Chemical Looping Technology and Its Fossil Energy Conversion Applications. *Industrial & Engineering Chemistry Research*. **2010,** 49, 10200-10211.
(15) Wang, I.; Ji, G.; Turap, Y.; Nie, H.; Li, Z.; Zhao, M.; Wang, W. A Short-Cut Chemical Looping Hydrogen Generation System by Using Iron-Based Material from Steel Industry. *Chem. Eng. J.* **2020**, 124882.
(16) Ugwu, A.; Donat, F.; Zaabout, A.; Müller, C.; Albertsen, K.; Cloete, S.; van Diest, G.; Amini, S. Hydrogen Production by Water Splitting Using Gas Switching Technology. *Powder Technology*. **2020,** 370, 48-63.
(17) Stenberg, V.; Rydén, M.; Mattisson, T.; Lyngfelt, A. Exploring Novel Hydrogen Production Processes by Integration of Steam Methane Reforming with Chemical-Looping Combustion (CLC-SMR) and Oxygen Carrier Aided Combustion (OCAC-SMR). *International Journal of Greenhouse Gas Control*. **2018,** 74, 28-39.
(18) Mei, D.; Soleimanisalim, A. H.; Linderholm, C.; Lyngfelt, A.; Mattisson, T. Reactivity and Lifetime Assessment of an Oxygen Releasable Manganese Ore with Biomass Fuels in a 10 kWth Pilot Rig for Chemical Looping Combustion. *Fuel Processing Technology*. **2021,** 215, 106743.
(19) Kidambi, P. R.; Cleeton, J. P.; Scott, S. A.; Dennis, J. S.; Bohn, C. D. Interaction of Iron Oxide with Alumina in a Composite Oxygen Carrier during the Production of Hydrogen by Chemical Looping. *Energy & fuels*. **2012,** 26, 603-617.

(20) Chan, M. S.; Liu, W.; Ismail, M.; Yang, Y.; Scott, S. A.; Dennis, J. S. Improving Hydrogen Yields, and Hydrogen: Steam Ratio in the Chemical Looping Production of Hydrogen Using $Ca_2Fe_2O_5$. *Chem. Eng. J.* **2016,** 296, 406-411.
(21) Abad, A.; Gayán, P.; Pérez-Vega, R.; García-Labiano, F.; de Diego, L.; Mendiara, T.; Izquierdo, M.; Adánez, J. Evaluation of Different Strategies to Improve the Efficiency of Coal Conversion in a 50 kWth Chemical Looping Combustion Unit. *Fuel*. **2020,** 271, 117514.
(22) Ortiz, M.; Gayán, P.; Luis, F.; García-Labiano, F.; Abad, A.; Pans, M. A.; Adánez, J. Hydrogen Production with CO_2 Capture by Coupling Steam Reforming of Methane and Chemical-Looping Combustion: Use of an Iron-Based Waste Product as Oxygen Carrier Burning a PSA Tail Gas. *Journal of Power Sources*. **2011,** 196, 4370-4381.
(23) Bhavsar, S.; Isenberg, N.; More, A.; Veser, G. Lanthana-Doped Ceria as Active Support for Oxygen Carriers in Chemical Looping Combustion. *Applied Energy*. **2016,** 168, 236-247.
(24) Galinsky, N. L.; Shafiefarhood, A.; Chen, Y.; Neal, L.; Li, F. Effect of Support on Redox Stability of Iron Oxide for Chemical Looping Conversion of Methane. *Applied Catalysis B: Environmental*. **2015,** 164, 371-379.
(25) Zeng, D.; Kang, F.; Qiu, Y.; Cui, D.; Li, M.; Ma, L.; Zhang, S.; Xiao, R. Iron Oxides with Gadolinium-Doped Cerium Oxides as Active Supports for Chemical Looping Hydrogen Production. *Chem. Eng. J.* **2020,** 396, 125153.
(26) Zhang, Y.; Kong, F.; Tong, A.; Fan, L.-S. Autothermal Operation Strategies of Chemical Looping Processes for Hydrogen Generation: Process Simulation, Parametric Studies, and Exergy Analysis. *Industrial & Engineering Chemistry Research*. **2020,** 59, 5877-5890.
(27) Zhao, Z.; Uddi, M.; Tsvetkov, N.; Yildiz, B.; Ghoniem, A. F. Redox Kinetics Study of Fuel Reduced Ceria for Chemical-Looping Water Splitting. *The Journal of Physical Chemistry C*. **2016,** 120, 16271-16289.
(28) Wang, L.; Shen, L.; Jiang, S.; Liu, W. Inhibition of Carbon Deposition Using Iron Ore Modified by K and Cu in Chemical Looping Hydrogen Generation. *International Journal of Energy Research*. **2019,** 43, 167-180.
(29) Riley, J.; Siriwardane, R.; Tian, H.; Benincosa, W.; Poston, J. Particle Scale Modeling of $CuFeAlO_4$ during Reduction with CO in Chemical Looping Applications. *Applied Energy*. **2019,** 251, 113178.
(30) Zhu, M.; Chen, S.; Soomro, A.; Hu, J.; Sun, Z.; Ma, S.; Xiang, W. Effects of Supports on Reduction Activity and Carbon Deposition of Iron Oxide for Methane Chemical Looping Hydrogen Generation. *Applied Energy*. **2018,** 225, 912-921.
(31) Kierzkowska, A.; Bohn, C.; Scott, S.; Cleeton, J.; Dennis, J.; Muller, C. Development of Iron Oxide Carriers for Chemical Looping Combustion Using Sol−Gel. *Industrial & Engineering Chemistry Research*. **2010,** 49, 5383-5391.
(32) Li, F.; Luo, S.; Sun, Z.; Bao, X.; Fan, L.-S. Role of Metal Oxide Support in Redox Reactions of Iron Oxide for Chemical Looping Applications: Experiments and Density Functional Theory Calculations. *Energy & Environmental Science*. **2011,** 4, 3661-3667.
(33) Gu, Z.; Li, K.; Qing, S.; Zhu, X.; Wei, Y.; Li, Y.; Wang, H. Enhanced Reducibility and Redox Stability of Fe_2O_3 in the Presence of CeO_2 Nanoparticles. **2014,** 4, 47191-47199.
(34) Yamaguchi, D.; Tang, L.; Wong, L.; Burke, N.; Trimm, D.; Nguyen, K.; Chiang, K. Hydrogen Production through Methane–Steam Cyclic Redox Processes with Iron-Based Metal Oxides. **2011,** 36, 6646-6656.
(35) Rydén, M.; Arjmand, M. Continuous Hydrogen Production via the Steam–Iron Reaction by Chemical Looping in a Circulating Fluidized-Bed Reactor. **2012,** 37, 4843-4854.

(36) Galinsky, N. L.; Huang, Y.; Shafiefarhood, A.; Li, F. Iron Oxide with Facilitated O^{2-} Transport for Facile Fuel Oxidation and CO_2 Capture in a Chemical Looping Scheme. *ACS Sustainable Chemistry Engineering*. **2013,** 1, 364-373.
(37) Cho, W. C.; Lee, J. K.; Nam, G. D.; Kim, C. H.; Cho, H.-S.; Joo, J. H. Degradation Analysis of Mixed Ionic-Electronic Conductor-Supported Iron-Oxide Oxygen Carriers for Chemical-Looping Conversion of Methane. *Applied Energy*. **2019,** 239, 644-657.
(38) Qin, L.; Cheng, Z.; Guo, M.; Xu, M.; Fan, J. A.; Fan, L.-S. Impact of 1% Lanthanum Dopant on Carbonaceous Fuel Redox Reactions with an Iron-Based Oxygen Carrier in Chemical Looping Processes. *ACS Energy Letters*. **2017,** 2, 70-74.
(39) Qin, L.; Guo, M.; Cheng, Z.; Xu, M.; Liu, Y.; Xu, D.; Fan, J. A.; Fan, L.-S. Improved Cyclic Redox Reactivity of Lanthanum Modified Iron-Based Oxygen Carriers in Carbon Monoxide Chemical Looping Combustion. *J. Mater. Chem. A*. **2017,** 5, 20153-20160.
(40) Chen, Y.-Y.; Guo, M.; Kim, M.; Liu, Y.; Qin, L.; Hsieh, T.-L.; Fan, L.-S. Predictive Screening and Validation on Chemical Looping Oxygen Carrier Activation by Tuning Electronic Structures via Transition Metal Dopants. *Chem. Eng. J.* **2021,** 406, 126729.
(41) Kresse, G.; Furthmüller, J. Efficiency of Ab-Initio Total Energy Calculations for Metals and Semiconductors Using a Plane-Wave Basis Set. *Computational materials science*. **1996,** 6, 15-50.
(42) Blöchl, P. E. Projector Augmented-Wave Method. **1994,** 50, 17953.
(43) Perdew, J. P.; Burke, K.; Ernzerhof, M. Generalized Gradient Approximation Made Simple. *Physical review letters*. **1996,** 77, 3865.
(44) Anisimov, V. I.; Zaanen, J.; Andersen, O. K. Band Theory and Mott insulators: Hubbard U instead of Stoner I. *Physical Review B*. **1991,** 44, 943.
(45) Jain, A.; Hautier, G.; Moore, C. J.; Ong, S. P.; Fischer, C. C.; Mueller, T.; Persson, K. A.; Ceder, G. A High-Throughput Infrastructure for Density Functional Theory Calculations. *Computational Materials Science*. **2011,** 50, 2295-2310.
(46) Henkelman, G.; Uberuaga, B. P.; Jónsson, H. A Climbing Image Nudged Elastic Band Method for Finding Saddle Points and Minimum Energy Paths. *The Journal of chemical physics*. **2000,** 113, 9901-9904.
(47) Lu, J.; Qiao, L.; Fu, P.; Wu, Y. Phase Equilibrium of Bi_2O_3–Fe_2O_3 Pseudo-Binary System and Growth of $BiFeO_3$ Single Crystal. *Journal of Crystal Growth*. **2011,** 318, 936-941.
(48) Palai, R.; Katiyar, R.; Schmid, H.; Tissot, P.; Clark, S.; Robertson, J.; Redfern, S.; Catalan, G.; Scott, J. β Phase and γ−β Metal-Insulator Transition in Multiferroic $BiFeO_3$. *Physical Review B*. **2008,** 77 (1), 014110.
(49) Dychalska, A.; Popielarski, P.; Franków, W.; Fabisiak, K.; Paprocki, K.; Szybowicz, M. Study of CVD Diamond Layers with Amorphous Carbon Admixture by Raman Scattering Spectroscopy. *Materials Science-Poland*. **2015,** 33 (4), 799-805.
(50) Bare, S. R.; Vila, F.; Charochak, M. E.; Prabhakar, S.; Bradley, W. J.; Jaye, C.; Fischer, D. A.; Hayashi, S.; Bradley, S. A.; Rehr, J. Characterization of Coke on a Pt-Re/γ-Al_2O_3 Re-Forming Catalyst: Experimental and Theoretical Study. *ACS Catalysis*. **2017,** 7, 1452-1461.
(51) Bouwmeester, H. J.; Song, C.; Zhu, J.; Yi, J.; van Sint Annaland, M.; Boukamp, B. A. A Novel Pulse Isotopic Exchange Technique for Rapid Determination of the Oxygen Surface Exchange Rate of Oxide Ion Conductors. *Physical chemistry chemical physics*. **2009,** 11, 9640-9643.
(52) Mudry, S.; Shtablavyi, I.; Liudkevych, U.; Winczewski, S. Structure and Thermal Expansion of Liquid Bismuth. *Mater. Sci.-Pol*. **2015,** 33, 767-773.

SYNOPSIS. Bismuth modifier forms a liquid metal shell that effectively enhances the redox activity and coke resistance of iron oxide based redox catalysts